Pressure-induced 1T to 3R structural phase transition in metallic VSe$_2$: X-ray diffraction and first-principles theory

Srishti Pal [1,*] Koyendrila Debnath,[2,*] Satyendra Nath Gupta,[1] Luminita Harnagea [3] D. V. S. Muthu [1]
Umesh V. Waghmare,[2] and A. K. Sood [1,†]

[1]*Department of Physics, Indian Institute of Science, Bengaluru 560012, India*
[2]*Theoretical Sciences Unit, Jawaharlal Nehru Centre for Advanced Scientific Research, Bengaluru 560064, India*
[3]*Department of Physics, Indian Institute of Science Education and Research, Pune 411008, India*

We study pressure-induced structural evolution of vanadium diselenide (VSe$_2$), a 1T polymorphic member of the transition metal dichalcogenide (TMD) family, using synchrotron-based powder x-ray diffraction (XRD) and first-principles density functional theory (DFT). Our XRD results reveal anomalies at $P \sim 4$ GPa in the c/a ratio, V-Se bond length, and Se-V-Se bond angle, signaling an isostructural transition. This transition is followed by a first-order structural transition from the 1T (space group $P\bar{3}m1$) phase to a 3R (space group $R\bar{3}m$) phase at $P \sim 11$ GPa due to sliding of adjacent Se-V-Se layers. Both the transitions at ~ 4 and 11 GPa are cognate with associated changes in the Debye-Waller factors not reported so far. We present various scenarios to understand the experimental results within DFT and find that the 1T to 3R transition is captured using spin-polarized calculations with Hubbard correction ($U_{\text{eff}} = U - J = 8$ eV), giving a transition pressure of ~ 9 GPa, close to the experimental value.

I. INTRODUCTION

Layered quasi-two-dimensional (quasi-2D) transition metal dichalcogenides (TMDs; MX_2, M = transition metals, Mo, W, V, Ta, Ti, Mn, etc., X = chalcogens, S, Se, Te, etc.) are being pursued intensely due to their emergent properties and significant applications [1–5]. One of the interesting features of bulk MX_2 compounds is their crystallization into different polytypes (viz., 1T, 2H, 3R, 1T', T_d, etc.) depending on the coordination of the nearest-neighbor chalcogen polyhedra around the transition metal and the various stacking sequences of the 2D layers in the (001) direction [6–10]. A TMD monolayer is composed of a sandwiched hexagonal layer of transition metal atoms between two hexagonal layers of chalcogens. These covalently bonded X-M-X slabs are then stacked in the vertical c direction with a weak van der Waals bond between them, resulting in an anisotropic three-dimensional (3D) structure. The trigonal 1T polytype with standard CdI$_2$ structure with space group $P\bar{3}m1$, the only stable structure of VSe$_2$ in ambient conditions [11–13], belongs to a regular octahedral coordination of six Se atoms around the central vanadium and a stacking sequence aBc (where a, b, and c label Se atomic layers and A, B, and C label V atomic layers) of Se-V-Se monolayers without any lateral shift [Fig. 1(a)]. The 3R polytype also has the same regular octahedral configuration but with a lateral shift between three successive Se-V-Se layers [$aBc\ bCa\ cAb$ stacking; Fig. 1(b)].

Unlike the semiconducting 2H polytypes, the 1T bulk VSe$_2$ is metallic due to significant overlaps between vana-

dium d bands and selenium p bands and shows a charge density wave (CDW) state [14,15]. 1T-VSe$_2$ is unique in the formation of a 3D chiral CDW [12,16,17] due to the partial nesting of its Fermi surface [18,19]. X-ray and electron diffraction studies [20,21] have established periodic lattice deformation to be the key precursor to this CDW transition to an incommensurate phase below 110 K and to a $4a' \times 4a'$ commensurate superlattice structure below 80 K (which is still incommensurate along the c axis with $c' \approx 3c$). The CDW transition of 1T-VSe$_2$ is very sensitive to any external perturbation that directly affects its electronic band structure. While the effects of reduced thickness down to the monolayer limit [1,3,22–24] or intercalation by Na, K, Cs, etc. [25–27], or interstitial vanadium itself [28] have been studied, there is limited work on the electronic and structural stability of VSe$_2$ under external pressure. While a large number of TMD crystals like 2H_c-MoS$_2$, MoSe$_2$, and WSe$_2$ exhibit pressure-induced metallization followed by an isostructural transformation of the crystal to 2H_a (except for 2H_c-MoSe$_2$) [29–32], a few others show a crystal symmetry change, e.g., transformation of trigonal 1T-TiS$_2$ to an orthorhombic phase at 16.2 GPa [33], a cubic to orthorhombic transition of MnS$_2$ [34], and the appearance of the monoclinic phase in 1T-IrTe$_2$ at 5 GPa, followed by the transition to a cubic phase at 20 GPa [35].

Friend *et al.* [36] reported high-pressure resistivity and Hall studies on bulk 1T-VSe$_2$ up to 3 GPa which showed an increase of the CDW transition temperature T_C with $\frac{dT_C}{dP} \sim 0.8$ K GPa^{-1} due to pressure broadening of the vanadium d-conduction band. Recently, using crystals from the same batch as used in the present study, Sahoo *et al.* [37] showed pressure enhancement of the CDW T_C in bulk 1T-VSe$_2$ reaching 240 K at 12 GPa, followed by quenching of the CDW state

*These authors contributed equally to this work.
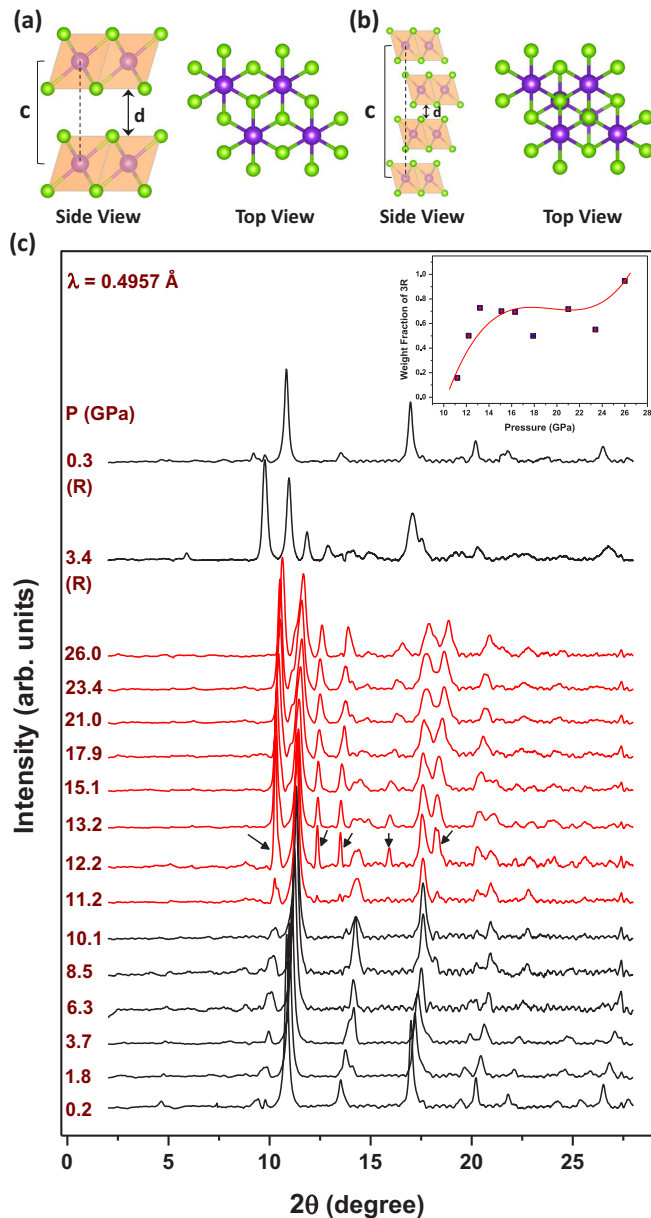†asood@iisc.ac.in

FIG. 1. Side and top views of (a) $1T$ ($P\bar{3}m1$) and (b) $3R$ ($R\bar{3}m$) crystal structures of VSe$_2$. (c) Angle dispersive XRD patterns during pressurization from 0.2 to 26.0 GPa (the two topmost patterns are after depressurizing to 0.3 GPa). Arrows indicate new peaks appearing at the onset of the first-order structural transition. The evolution of the weight fraction of the $3R$ phase with increasing pressure is shown in the inset.

before a final evolution into a superconducting phase with $T_C \sim 4$ K after 15 GPa. Recently, a report on high-pressure x-ray diffraction (XRD) and density functional theory (DFT) studies [38] indicated the new phase of VSe$_2$ after 12 GPa to be a $3 \times 3 \times 1$ supercell of monoclinic symmetry. Here we report high-pressure XRD and DFT calculations which are at variance with that recent report [38]. Our XRD data show a first-order structural transition to a $3R$ phase at $\sim$11 GPa. We also show an isostructural transition at $\sim$4 GPa, in agreement with recent reports [37,38], not only by the anomalous c/a

ratio but also by the changes in the V-Se bond length and Se-V-Se bond angle. Our XRD data and theoretical calculations are inconsistent with the monoclinic space group assignment of Ref. [38]. Our detailed DFT calculations do show a transition from $1T$ to $3R$ at $\sim$9 GPa, a pressure value very close to the experimental transition pressure of 11 GPa. Notably, the thermal Debye Waller factors of selenium atoms increase by a factor of $\sim$4 across the structural phase transition.

II. EXPERIMENTAL AND COMPUTATIONAL DETAILS

Single crystals of VSe$_2$ were grown using a chemical vapor transport technique using iodine as the transporting agent. The crystal structure, purity, crystal quality, morphology, and chemical composition of the single crystals were determined using x-ray powder diffraction (Bruker D8 diffractometer: Cu $K\alpha$ radiation), Laue diffraction, and scanning electron microscope (ZEISS GeminiSEM 500) equipped with an energy dispersive x-ray spectroscopy probe. The samples proved to be homogeneous, with a V:Se ratio of 1:2 within the error bars of the techniques (1–2 at. %). The electrical characterization of the crystals was reported in our recent work [37].

Single crystals of $1T$-VSe$_2$ were powdered and loaded inside a Mao-Bell-type diamond anvil cell (DAC). The DAC had two 16-facet brilliant cut diamonds with an $\sim$600 μm culet diameter to pressurize the sample placed inside a stainless-steel gasket hole $\sim$200 μm in diameter. Ruby fluorescence was used to calibrate the applied pressure [39]. A 4:1 methanol-ethanol mixture with a freezing pressure of $\sim$10.4 GPa [40] was used to transmit the pressure through the sample.

The angle dispersive synchrotron XRD study on $1T$-VSe$_2$ was carried out at Elettra, Italy, using the Xpress beamline with $\lambda = 0.4957$ Å from 0.2 to 26 GPa at room temperature. Data were recorded using a MAR 345 image plate. A standard LaB$_6$ crystal was used to calibrate the sample to detector distance and orientation angles of the detector. The selected area 2D diffraction pattern was processed using FIT2D software [41] for conversion to a one-dimensional 2θ vs intensity plot. The raw data for the entire pressure range from 0.2 to 26 GPa were fitted using the standard Rietveld refinement procedure in the GSAS software package [42].

Our first-principles calculations are based on DFT as implemented in the QUANTUM ESPRESSO package [43], in which we treat only the valence electrons by replacing the potential of ionic cores with pseudopotentials. The exchange-correlation energy of electrons is treated within a generalized gradient approximation (GGA) [44] with a functional form parametrized by Perdew, Burke, and Ernzerhof (PBE) [45]. Electronic wave functions and charge density were represented in plane wave basis sets truncated at energy cutoffs of 60 and 500 Ry, respectively. Brillouin zone (BZ) integrations were sampled on uniform dense $24 \times 24 \times 12$ and $24 \times 24 \times 6$ meshes of k points for $1T$ and $3R$ structures of VSe$_2$, respectively. The discontinuity in occupation numbers of electronic states was smeared using a Fermi-Dirac distribution function with a broadening temperature of $k_B T = 0.003$ Ry. We include van der Waals (vdW) interaction using the PBE+D2 method of Grimme [46]. Dynamical matrices were calculated within the density functional perturbation

theory [47] on a $2 \times 2 \times 2$ mesh in the Brillouin zone. We Fourier interpolated these dynamical matrices to obtain the phonon frequencies at arbitrary wave vectors and dispersion along the high-symmetry lines in the Brillouin zone. We also performed first-principles calculations using the projected augmented wave method [48,49] as implemented in the Vienna Ab initio Simulation Package (VASP) [50,51]. Spin-polarized calculations were performed using the PBE functional for the exchange-correlation term, with the Hubbard parameter correction GGA+U introduced by Dudarev *et al.* [52,53], in which the parameters U and J do not enter separately and only the difference $(U - J)$ is relevant ($U_{eff} = U - J = 8.0$ eV). The plane wave basis was truncated at a kinetic energy cutoff of 36.75 Ry. Maximum force on ions in the relaxed structure was within a threshold of 10^{-4} eV/Å. BZ integrations were sampled on dense $24 \times 24 \times 12$, $24 \times 24 \times 24$, and $5 \times 24 \times 8$ meshes of k points for 1T, 3R (primitive unit cell considered), and recently reported [38] $C2/m$ structures of VSe$_2$, respectively. Also, for the sake of comparison, a sparse $8 \times 8 \times 3$ mesh of k points was used in sampling BZ integrations in calculations of the 1T and $C2/m$ structures shown in Sec. VII of the Supplemental Material (SM) [54], similar to the recent report [38], and an $8 \times 8 \times 8$ mesh was used in the calculation of the 3R structure (primitive unit cell considered).

III. RESULTS AND DISCUSSION

Angle dispersive powder XRD patterns of VSe$_2$ at room temperature at selected pressure values are stacked in Fig. 1(c). The ambient trigonal phase with space group $P\bar{3}m1$ (No. 164), $z = 1$, exhibits stability up to ~10.1 GPa, above which new peaks start to appear in the diffraction pattern at ~10.3°, 12.3°, 13.5°, 15.9°, 18.3°, 20.3°, 22.1°, and 23.8° and are prominent in intensity from 12.2 GPa [marked by arrows in Fig. 1(c)] onwards. The emergence of new Bragg reflections over the existing ones confirms the occurrence of new crystal symmetry coexisting with the previous 1T phase [the weight fraction of the 3R phase with increasing pressure is shown in the inset of Fig. 1(c)].

The new high-pressure phase has been indexed unambiguously to a standard CdCl$_2$ rhombohedral 3R structure with a space group symmetry of $R\bar{3}m$ (No. 166), $z = 3$. This is in contrast to the high-pressure pattern reported by Sereika *et al.* [38] showing the onset of only small shoulder peaks above 15.5 GPa which were indexed based on $C2/m$ (a subgroup of $P\bar{3}m1$) monoclinic superstructure. It should be noted that interaction of the nonhydrostatic environment above ~10 GPa offered by the 4:1 methanol-ethanol mixture used as the pressure transmitting medium (PTM) in the present study, compared to the hydrostatic pressure medium (neon gas) in Ref. [38], with the VSe$_2$ sample cannot be ruled out to induce a different high-pressure structure in the system. Also, since the material VSe$_2$ is very prone to growing vanadium rich [36,37,55], the difference in the quality of the samples used in the two studies is another possible reason behind the discrepancies in the high-pressure structures. The highest-pressure XRD pattern in Fig. 1(c) confirms that the 1T to 3R transition in VSe$_2$ is incomplete even at our highest measured pressure of ~26 GPa, where the two phases still
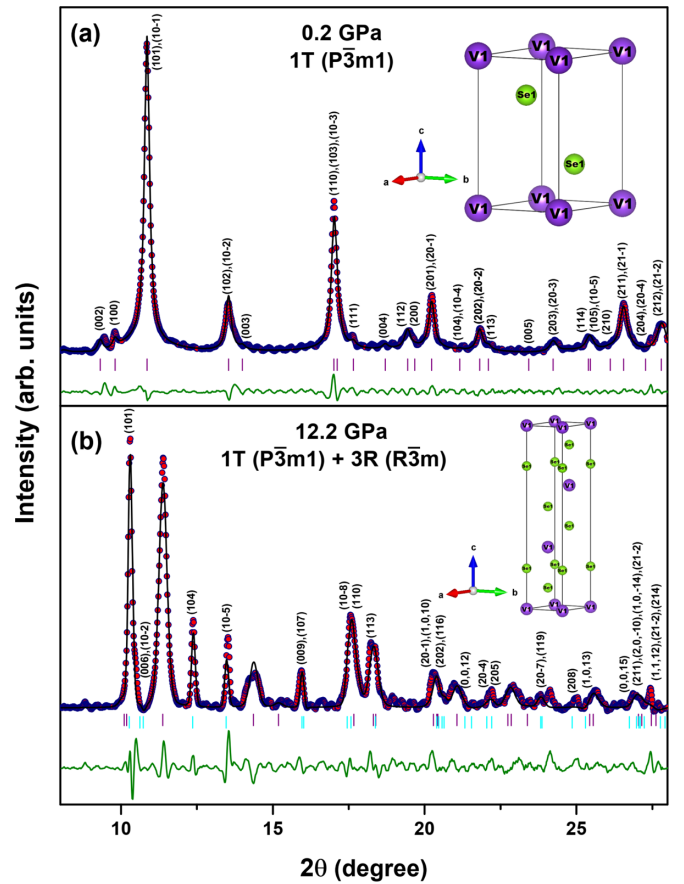

FIG. 2. (a) and (b) Rietveld refined XRD patterns at 0.2 and 12.2 GPa, respectively, matched with $P\bar{3}m1$ (No. 164) and a mixture of $P\bar{3}m1$ (No. 164) and $R\bar{3}m$ (No. 166). Experimental data are indicated by solid circles. The calculated pattern is drawn as a black solid line. Reflection positions for the 1T phase are indicated by magenta vertical bars, and those for 3R are indicated by cyan ones. The lower dark green curve is the weighted difference between observed and calculated profiles. The unit cells including atoms are shown in the inset.

coexist. Also, the structural transition of VSe$_2$ is found to be reversible, but with the existence of a large hysteresis of about 8 GPa, as indicated by the two topmost patterns in Fig. 1(c).

Figure 2 shows the Rietveld refined fitted patterns at 0.2 and 12.2 GPa using $P\bar{3}m1$ (1T) and a mixture of $P\bar{3}m1$ (1T) and $R\bar{3}m$ (3R), respectively. Two equivalent representations exist for the 3R crystal structure, i.e., using rhombohedral axes, leading to the primitive cell (V), or using hexagonal axes, leading to a unit cell having a volume three times ($3V$) larger than the primitive one. We have adopted the hexagonal axes since they clearly evince the difference between the stacking sequence of the Se-V-Se trilayers in the 1T and 3R polytypes as depicted in Figs. 1(a) and 1(b). The Rietveld refined parameters, including the lattice constants, cell volume, atomic positions of V and Se atoms (in terms of fractional coordinates), V-Se bond length, interlayer distance d, and the reduced χ^2 and profile R_p factors, are listed in Table I.

Variation in the lattice parameters a and c and the c/a ratio with increasing pressure [see Figs. 3(b)–3(d)] reveals that the c/a ratio of the 1T phase decreases up to 10.1 GPa, indicating

TABLE I. Rietveld refined parameters.

	0.2 GPa (1T)	12.2 GPa (1T)	12.2 GPa (3R)
Space group	$P\bar{3}m1$ ($z = 1$)	$P\bar{3}m1$ ($z = 1$)	$R\bar{3}m$ ($z = 3$)
a (Å)	3.349998	3.226370	3.244756
c (Å)	6.101036	5.628404	16.073330
V/f.u. (Å^3)	59.296	50.739	48.852
V (X, Y, Z)	(0,0,0)	(0,0,0)	(0,0,0)
Se (X, Y, Z)	$(\frac{1}{3}, \frac{2}{3}, 0.268636)$	$(\frac{1}{3}, \frac{2}{3}, 0.268636)$	$(0,0,0.221085)$
V-Se (Å)	2.5352	2.3863	2.6009
d (Å)	2.823120	2.645507	1.749368
Reduced χ^2	5.31		8.50
Profile R_p	14.09%		21.22%

the higher compressibility of the c axis in contrast to that of the a (or b) axis, giving prominent anisotropy of the crystal which can be attributed to the relative strengths of the weak interlayer van der Waals bond and strong intralayer covalent bonds. In contrast, the c/a ratio becomes almost constant after 11 GPa in the 3R phase (excluding the highest pressure value). This can be explained by the interlayer d spacing and the V-Se bond length of the 3R phase compared to those of 1T at 12.2 GPa (Table I). A reduced interlayer separation and a higher V-Se bond length of the 3R phase tunes the interplay between the intralayer covalent and interlayer van der Waals couplings, resulting in suppression of the 2D character of the system, making it more isotropic and thus giving rise to an almost flat c/a ratio with increasing pressure.

The volume per formula unit for each phase was determined [see Fig. 3(a)] against pressure for the entire range to get the P-V relation for both phases. The finite volume discontinuity at $\sim$11 GPa confirms the first-order nature of this structural transition, which is also corroborated by a large hysteresis ($\sim$8 GPa) in the transition pressure. The P-V data in each phase are fitted using the third-order Birch-Murnaghan (BM) equation of state [56], given by

$$P = \frac{3}{2}B_0\left[\left(\frac{V0}{V}\right)^{\frac{7}{3}} - \left(\frac{V_0}{V}\right)^{\frac{5}{3}}\right]$$
$$\times \left\{1 - \left(3 - \frac{3}{4}B_0'\right)\left[\left(\frac{V_0}{V}\right)^{\frac{2}{3}} - 1\right]\right\}, \quad (1)$$

where V_0 denote the zero-pressure cell volume (per formula unit), B_0 is the zero-pressure bulk modulus, and B_0' is its pressure derivative. In order to get an unambiguous value of these parameters, the BM equation can be linearized and cast in terms of reduced pressure $H = \frac{P}{3f(1+2f)^{5/2}}$ and Eulerian strain $f = \frac{1}{2}(X^2 - 1)$, where $X = (\frac{V}{V_0})^{-1/3}$, as [57]

$$H = B_0 + \frac{3}{2}B_0(B_0' - 4)f. \quad (2)$$

The linear fits for the f vs H plots shown in the inset of Fig. 3(a) estimate the fitting parameters as $B_0 = 23.8 \pm 0.8$ GPa, $B_0' = 16.6 \pm 1.0$ in the 1T phase and $B_0 = 55.8 \pm 2.0$ GPa, $B_0' = 5.7 \pm 0.4$ in the 3R phase. These parameters guide us to the fitting of P-V data using the BM equation of state, giving $V_0 = 59.4 \pm 0.1$ Å^3, $B_0 = 23.9 \pm 0.8$ GPa, and $B_0' = 16.6$ (fixed) in the 1T phase and $V_0 = 56.1 \pm 0.3$ Å^3,
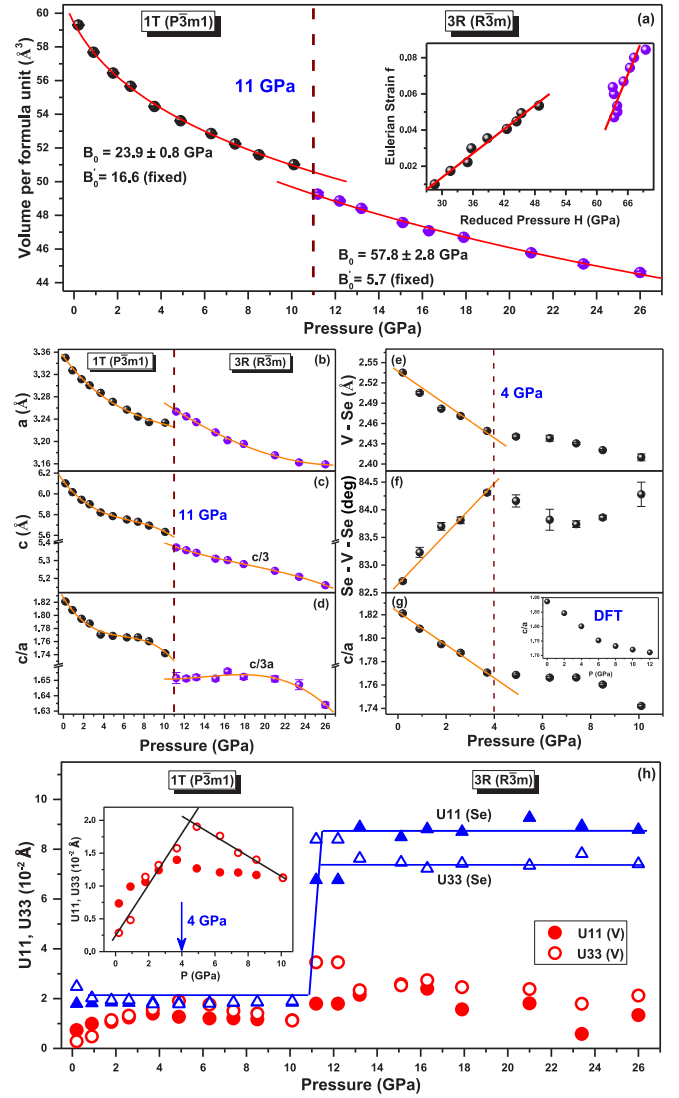

FIG. 3. (a) Fitted (red solid line) P-V diagram using the third-order BM equation of state. The inset shows Eulerian strain f vs reduced pressure H plots in the two phases. (b)–(d) Pressure dependence of lattice parameters a, c, and the c/a ratio for 1T and 3R phases. (e)–(g) Pressure variation of the V-Se bond length, Se-V-Se bond angle, and c/a ratio of the 1T phase (the orange solid lines are a guide to the eye). The inset of (g) shows the pressure dependence of c/a from DFT calculations. (h) Pressure evolution of the $U11$ and $U33$ components of the Debye-Waller temperature factors for the V and Se atoms. The inset of (h) shows the subtle anomaly in the U parameters of the V atom across the isostructural transition at 4 GPa.

$B_0 = 57.8 \pm 2.8$ GPa, and $B_0' = 5.7$ (fixed) in the 3R phase. We may note that, although the value obtained for B_0' (=16.6) in the 1T phase is high compared to that of other TMD compounds, for which it typically ranges from 4 to 11, a similar high value of 16.3 for B_0' was previously reported for pyrite-type MnTe$_2$ [58]. We do not detect any change in the value of B_0 of the 1T phase around 6 GPa as reported by Sereika *et al.* [38]. However, as shown in Figs. 3(e)–3(g), the pressure dependence of the V-Se bond length, Se-V-Se bond angle, and c/a ratio of the 1T phase shows a significant change, making
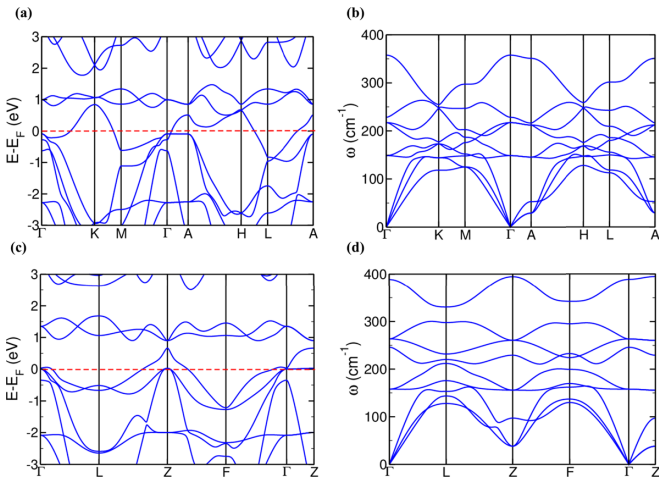
FIG. 4. (a) Electronic structure and (b) phonon dispersion of $1T$-VSe$_2$ (space group: $P\bar{3}m1$) at 0 GPa. (c) Electronic structure and (d) phonon dispersion of $3R$-VSe$_2$ (space group: $R\bar{3}m$) at 12 GPa.

an isostructural transition at ~4 GPa, in agreement with recent reports [37,38].

The pressure effects on the Debye-Waller factor [59,60] U_{ij}, a measure of the mean-square thermal displacement of an atom from its equilibrium position due to crystal lattice vibrations, have not been studied yet in diffraction measurements. Figure 3(h) shows the pressure variation of the diagonal components $U11$ (=$U22$) and $U33$ of the thermal ellipsoid for the V and Se atoms in the $1T$ and $3R$ phases of VSe$_2$. The U parameters for the V atom in the $1T$ phase show subtle anomalous behavior [inset of Fig. 3(h)] across the isostructural transition pressure of ~4 GPa. In the $3R$ phase, the U parameters for the V atoms do not show any significant variation. Notably, in contrast, for the Se atoms, both U parameters $U11$ and $U33$ remain almost constant in the $1T$ phase but show an abrupt increase (~4 times) in the $3R$ phase. In this regard, we may note that the abrupt change in the U parameters across the 11 GPa transition cannot be taken care of by the phase fraction of $1T$ and $3R$ phases (see SM [54], Sec. III).

We now present our first-principles computational methods to understand the structural evolution in VSe$_2$. Our calculations reproduce the metallic nature of ambient $1T$-VSe$_2$ ($P\bar{3}m1$), as shown in Fig. 4(a). Our estimates of the optimized lattice constants of $1T$-VSe$_2$ at 0 GPa are $a = 3.35$ Å and $c = 6.12$ Å, in close agreement with our experimental values ($a = 3.35$ Å and $c = 6.10$ Å). The phonon dispersion [Fig. 4(b)] of $1T$-VSe$_2$ at 0 GPa confirms its local stability as no imaginary frequencies were observed. $3R$-VSe$_2$ ($R\bar{3}m$) is metallic at 12 GPa since the valence band maxima and conduction band minima overlap [Fig. 4(c)]. Optimized lattice parameters obtained from our first-principles calculation using Grimme's D2 van der Waals correction at 12 GPa are $a = 3.16$ Å and $c = 17.39$ Å, where the c value is overestimated compared with the experimental values ($a = 3.24$ Å and $c = 16.07$ Å). The $R\bar{3}m$ phase is dynamically stable with no unstable phonon modes in its phonon dispersion [Fig. 4(d)]. Lattice parameters of $1T$-VSe$_2$ vary smoothly as a function of hydrostatic pressure up to P ~12 GPa, with a notable change

in the slope of the c/a ratio with pressure at $P_C \sim 6$ GPa [inset of Fig. 3(g)], suggesting an isostructural phase transition, consistent with our experimental results and the recent report [38].

To explore the possibility of a pressure-dependent phase transition from the $1T$ to $3R$ structure of VSe$_2$, we have determined the changes in enthalpy of these structures but did not observe any transition from the $1T$ to $3R$ phase (see the SM [54], Fig. S4). VSe$_2$ is a layered material which has a strong covalent bonding within the layer and weak van der Waals interaction between the layers. In this regard, we compared the lattice parameters of $3R$ with experiments obtained using different flavors of the van der Waals correction and London s6 forces and introduced Hubbard U parameter of 1 eV [52] to include on-site correlations of d electrons of the V atom. These results are presented in Table SII in the SM [54]. As we did not find a phase transition from the $1T$ to $3R$ structure under hydrostatic pressure, we investigated the stability of $2H_a$ (another polytype into which bulk dichalcogenides crystallize), having a hexagonal unit cell with $aBa\,cBc$ stacking and space group $P6_3/mmc$ [61,62]. Phonon dispersion at 12 GPa confirms that $2H_a$ is stable and has soft modes, indicating a possible phase transition. From the estimated difference in enthalpy, we do find a transition from $1T$ to $2H_a$ near P ~12 GPa. Although our theory predicts this phase transition, the $2H_a$ structure cannot be fitted to our XRD data at high pressures. We have also considered the $3R$ structure based on $2H_a$ stacking ($R3m$ space group with $aBa\,bCb\,cAc$ stacking). The relative stability of this $3R$ structure with respect to the $1T$ structure as seen from the difference in enthalpy does not reveal a phase transition (see the SM [54], Sec. V, for more information on the stability analysis of $2H_a$ and $3R$ ($R3m$)).

To examine whether the finite-temperature effects contribute to the stability of the $3R$ phase, we have evaluated temperature-dependent vibrational free energies of $1T$, $3R$ ($R\bar{3}m$), and $3R$ ($R3m$) structures. As is evident in the transition temperatures at various hydrostatic pressures (see the SM [54], Sec. VI, for details), the temperature that stabilizes $3R$ polytypes is not realistic, ruling out temperature effects.

Having examined all the above possibilities to stabilize the $3R$ phase established unambiguously in our XRD experiments, we obtain the energetics of $1T$ and $3R$ structures of VSe$_2$ with spin-polarized calculations using VASP including the Hubbard parameter correction GGA+U ($U_{\text{eff}} = U - J = 8.0$ eV). Sampling of BZ integrations was carried out on dense uniform $24 \times 24 \times 12$, $24 \times 24 \times 24$, and $5 \times 24 \times 8$ meshes of k points for $1T$, $3R$ (primitive unit cell considered), and $C2/m$ structures of VSe$_2$, respectively. Calculated enthalpies of $1T$, $3R$, and $C2/m$ phases as a function of pressure are plotted in Fig. 5. Surprisingly, the present DFT calculations predict the monoclinic $C2/m$ structure is the ground state of the VSe$_2$ system at $P = 0$ GPa compared to the experimentally established ambient $1T$ phase. The $C2/m$ structure remains the lowest-energy structure of the system up to $P = 20$ GPa. Also, the absence of any crossover between the $1T$ and the $C2/m$ phases is at variance with the claim of Ref. [38] of obtaining a $1T$ to $C2/m$ transition at ~15.5 GPa. The inset of Fig. 5 represents the difference in enthalpy between the $3R$ (space group: $R\bar{3}m$) and $1T$ (space group: $P\bar{3}m1$) structures of
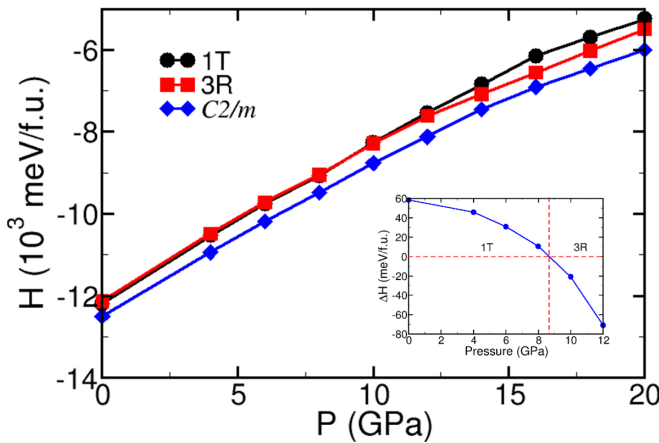
FIG. 5. Pressure dependence of enthalpies of the $1T$, $3R$, and $C2/m$ structures of VSe$_2$. The inset shows the difference in enthalpy between $3R$ (space group: $R\bar{3}m$) and $1T$ structures, indicating a phase transition from $1T$ to $3R$ structure of VSe$_2$ at $P \sim 9$ GPa.

VSe$_2$, revealing a phase transition from the $1T$ to $3R$ structure at $P \sim 9$ GPa.

The k meshes in the present study have been chosen appropriately to satisfy the inverse proportionality of the lattice constants in real space. Also, metallic systems require a dense set of k points due to the presence of a Fermi surface where the occupation of the bands changes rapidly from 0 to 1, thereby implying very high Fourier components in $F(k)$. However, the chosen k mesh of $8 \times 8 \times 3$ for the $1T$ and $C2/m$ structures in Ref. [38] is less dense and is, perhaps, inconsistent with their reported lattice parameters of $a = 15.98$ Å, $b = 3.07$ Å, and $c = 5.32$ Å. Still, for the sake of comparison, we have also performed the enthalpy calculations for $1T$, $3R$, and $C2/m$ structures using the k mesh selection of Ref. [38], and the results are given in Sec. VII of the Supplemental Material [54]. We still do not find any transition at ~ 15.5 GPa from the $1T$ to $C2/m$ phases as claimed in Ref. [38].

IV. CONCLUSIONS

To conclude, we address two pressure-driven transitions in bulk $1T$-VSe$_2$ using x-ray diffraction and DFT studies. The first transition around 4 GPa is isostructural with distinctive anomalies in the bond length, bond angle, c/a ratio, and Debye-Waller factors. The second transition around 11 GPa

is from the $1T$ ($P\bar{3}m1$) to $3R$ ($R\bar{3}m$) structure due to the sliding of the Se-V-Se trilayer, leading to a contraction of unit cell volume per formula unit by $\sim 3\%$. A similar layer sliding mechanism has also been seen in other TMD materials like MoS$_2$ [29,30] and WSe$_2$ [32]. Our high-pressure XRD data are inconsistent with the $C2/m$ monoclinic space group assignment by a recent report [38]. The possible reasons for this discrepancy are the differences in the pressure mediums and quality of the samples used in the two studies. Hence, further exploration of the system, preferably using different pressure-transmitting media, has potential for future studies. The $1T$ to $3R$ transition witnesses a relatively large jump in the thermal factors for the selenium atoms which can be related to both the disorder and the enhanced anharmonic interactions in the high-pressure phase. However, presently, we are not aware of any mechanism for enhanced disorder across the transition, which needs further investigation in the future. Our analysis based on first-principles calculations could confirm the stability of the $3R$ phase around 9 GPa only after incorporation of spin-polarized calculations to account for the Hubbard correction with $U_{\text{eff}} = U - J = 8$ eV. The present DFT calculations predict the $C2/m$ is the ground state structure of the VSe$_2$ system at $P = 0$ GPa. The inadequacy of the present DFT results in capturing the experimental $1T$ structure at $P = 0$ GPa needs further insight. Also, our DFT calculations are unable to capture a transition from $1T$ to a monoclinic superstructure phase above 15.5 GPa in the system using a sparse k mesh as used in Ref. [38] (see the SM [54], Sec. VII, for more information) as well as using a more appropriate and denser mesh of k points.

[1] Y. Umemoto, K. Sugawara, Y. Nakata, T. Takahashi, and T. Sato, Nano Res. **12**, 165 (2019).

[2] Z. Zhang, Y. Gong, X. Zou, P. Liu, P. Yang, J. Shi, L. Zhao, Q. Zhang, L. Gu, and Y. Zhang, ACS Nano **13**, 885 (2019).

[3] G. Duvjir, B. K. Choi, I. Jang, S. Ulstrup, S. Kang, T. T. Ly, S. Kim, Y. H. Choi, C. Jozwiak, A. Bostwick, E. Rotenberg, J.-G. Park, R. Sankar, K.-S. Kim, J. Kim, and Y. J. Chang, Nano Lett. **18**, 5432 (2018).

[4] Q. H. Wang, K. Kalantar-Zadeh, A. Kis, J. N. Coleman, and M. S. Strano, Nat. Nanotechnol. **7**, 699 (2012).

[5] G. Eda, T. Fujita, H. Yamaguchi, D. Voiry, M. Chen, and M. Chhowalla, ACS Nano **6**, 7311 (2012).

[6] A. A. Balchin, in *Crystallography and Crystal Chemistry of Materials with Layered Structures*, edited by F. Levy, Physics and Chemistry of Materials with Layered Structures Vol. 2 (D. Reidel Publishing Company, Dordrecht, Holland, 1976), p. 1.

[7] H. Katzke, P. Tolèdano, and W. Depmeier, Phys. Rev. B **69**, 134111 (2004).

[8] Y. Sun, S.-C. Wu, M. N. Ali, C. Felser, and B. Yan, Phys. Rev. B **92**, 161107(R) (2015).

[9] B. E. Bwnro, Acta Crystallogr. **20**, 268 (1966).

[10] J. Augustin, V. Eyert, T. Böker, W. Frentrup, H. Dwelk, C. Janowitz, and R. Manzke, Phys. Rev. B **62**, 10812 (2000).

[11] E. Rost and L. Gjertsen, Z. Anorg. Allg. Chem. **328**, 299 (1964).

[12] M. Bayard and M. J. Sienko, J. Solid State Chem. **19**, 325 (1976).

[13] F. Li, K. Tu, and Z. Chen, J. Phys. Chem. C **118**, 21264 (2014).

[14] H. W. Myron, Physica B+C (Amsterdam) **99**, 243 (1980).

[15] A. Zunger and A. J. Freeman, Phys. Rev. B **19**, 6001 (1979).

[16] W. Jolie, T. Knispel, N. Ehlen, K. Nikonov, C. Busse, A. Grüneis, and T. Michely, Phys. Rev. B **99**, 115417 (2019).

[17] S. Barua, M. C. Hatnean, M. R. Lees, and G. Balakrishnan, Sci. Rep. **7**, 10964 (2017).

[18] K. Terashima, T. Sato, H. Komatsu, T. Takahashi, N. Maeda, and K. Hayashi, Phys. Rev. B **68**, 155108 (2003).

[19] V. N. Strocov, M. Shi, M. Kobayashi, C. Monney, X. Wang, J. Krempasky, T. Schmitt, L. Patthey, H. Berger, and P. Blaha, Phys. Rev. Lett. **109**, 086401 (2012).

[20] K. Tsutsumi, Phys. Rev. B **26**, 5756 (1982).

[21] P. M. Williams, in *Crystallography and Crystal Chemistry of Materials with Layered Structures*, edited by F. Levy, Physics and Chemistry of Materials with Layered Structures Vol. 2 (D. Reidel Publishing Company, Dordrecht, Holland, 1976), Vol. 2 p. 51.

[22] P. Chen, W. W. Pai, Y.-H. Chan, V. Madhavan, M. Y. Chou, S.-K. Mo, A.-V. Fedorov, and T.-C. Chiang, Phys. Rev. Lett. **121**, 196402 (2018).

[23] A. H. M. A. Wasey, S. Chakrabarty, and G. P. Das, J. Appl. Phys. **117**, 064313 (2015).

[24] J. Yang, W. Wang, Y. Liu, H. Du, W. Ning, G. Zheng, C. Jin, Y. Han, N. Wang, Z. Yang, M. Tian, and Y. Zhang, Appl. Phys. Lett. **105**, 063109 (2014).

[25] H. E. Brauer, H. I. Starnberg, L. J. Holleboom, V. N. Strocov, and H. P. Hughes, Phys. Rev. B **58**, 10031 (1998).

[26] H. I. Starnberg, H. E. Brauer, L. J. Holleboom, and H. P. Hughes, Phys. Rev. Lett. **70**, 3111 (1993).

[27] I. Ekvall, H. E. Brauer, E. Wahlström, and H. Olin, Phys. Rev. B **59**, 7751 (1999).

[28] F. J. DiSalvo and J. V. Waszczak, Phys. Rev. B **23**, 457 (1981).

[29] A. P. Nayak, S. Bhattacharyya, J. Zhu, J. Liu, X. Wu, T. Pandey, C. Jin, A. K. Singh, D. Akinwande, and J.-F. Lin, Nat. Commun. **5**, 3731 (2014).

[30] Z.-H. Chi, X.-M. Zhao, H. Zhang, A. F. Goncharov, S. S. Lobanov, T. Kagayama, M. Sakata, and X.-J. Chen, Phys. Rev. Lett. **113**, 036802 (2014).

[31] Z. Zhao, H. Zhang, H. Yuan, S. Wang, Y. Lin, Q. Zeng, G. Xu, Z. Liu, G. K. Solanki, K. D. Patel, Y. Cui, H. Y. Hwang, and W. L. Mao, Nat. Commun. **6**, 7312 (2015).

[32] X. Wang, X. Chen, Y. Zhou, C. Park, C. An, Y. Zhou, R. Zhang, C. Gu, W. Yang, and Z. Yang, Sci. Rep. **7**, 46694 (2017).

[33] F. Yu, J.-X. Sun, and Y.-H. Zhou, Solid State Sci. **12**, 1786 (2010).

[34] T. Chattopadhyay, H. G. V. Schnering, and W. A. Grosshans, Physica B+C (Amsterdam) **139–140**, 305 (1986).

[35] J. M. Lègera, A. S. Pereiraa, J. Hainesa, S. Jobicb, and R. Brec, J. Phys. Chem. Solids **61**, 27 (2000).

[36] R. H. Friend, D. Jèrome, D. M. Schleich, and P. Moliniè, Solid State Commun. **27**, 169 (1978).

[37] S. Sahoo, U. Dutta, L. Harnagea, A. K. Sood, and S. Karmakar, Phys. Rev. B **101**, 014514 (2020).

[38] R. Sereika, C. Park, C. Kenney-Benson, S. Bandaru, N. J. English, Q. Yin, H. Lei, N. Chen, C.-J. Sun, S. M. Heald, J. Ren, J. Chang, Y. Ding, and H. Mao, J. Phys. Chem. Lett. **11**, 380 (2020).

[39] H. Mao, J. Xu, and P. Bell, J. Geophys. Res. **91**, 4673 (1986).

[40] G. J. Piermarini, S. Block, and J. D. Barnett, J. Appl. Phys. **44**, 5377 (1973).

[41] A. Hammersley, Computer program FIT2D, European Synchrotron Radiation Facility, Grenoble, 1997.

[42] A. C. Larson and R. B. Von Dreele, GSAS General Structure Analysis System, Los Alamos Natl. Laboratory Report No. LAUR 86-748 (2000).

[43] P. Giannozzi, S. Baroni, N. Bonini, M. Calandra, R. Car, C. Cavazzoni, D. Ceresoli, G. L. Chiarotti, M. Cococcioni, I. Dabo, A. D. Corso, S. de Gironcoli, S. Fabris, G. Fratesi, R. Gebauer, U. Gerstmann, C. Gougoussis, A. Kokalj, M. Lazzeri, L. Martin-Samos, N. Marzari, F. Mauri, R. Mazzarello, S. Paolini, A. Pasquarello, L. Paulatto, C. Sbraccia, S. Scandolo, G. Sclauzero, A. P Seitsonen, A. Smogunov, P. Umari, and R. M Wentzcovitch, J. Phys.: Condens. Matter **21**, 395502 (2009).

[44] X. Hua, X. Chen, and W. A. Goddard, Phys. Rev. B **55**, 16103 (1997).

[45] J. P. Perdew, K. Burke, M. Ernzerhof, Phys. Rev. Lett. **80**, 891 (1998).

[46] S. Grimme, J. Comput. Chem. **25**, 1463 (2004).

[47] S. Baroni, S. de Gironcoli, A. D. Corso, and P. Giannozzi, Rev. Mod. Phys. **73**, 515 (2001).

[48] P. E. Blöchl, Phys. Rev. B **50**, 17953 (1994).

[49] G. Kresse and D. Joubert, Phys. Rev. B **59**, 1758 (1999).

[50] G. Kresse and J. Furthmüller, Phys. Rev. B **54**, 11169 (1996).

[51] G. Kresse and J. Furthmüller, Comput. Mater. Sci. **6**, 15 (1996).

[52] S. L. Dudarev, G. A. Botton, S. Y. Savrasov, C. J. Humphreys, and A. P. Sutton, Phys. Rev. B **57**, 1505 (1998).

[53] S. Lutfalla, V. Shapovalov, and A. T. Bell, J. Chem. Theory Comput. **7**, 2218 (2011).

[54] See Supplemental Material at http://link.aps.org/supplemental/10.1103/PhysRevB.104.014108 for additional results from powder x-ray diffraction and density functional theoretical calculations.

[55] D. J. Eagleshamt, R. L. Witherst, and D. M. Bird, J. Phys. C **19**, 359 (1986).

[56] F. Birch, J. Geophys. Res. **91**, 4949 (1986).

[57] R. J. Angel, Rev. Mineral. Geochem. **41**, 35 (2000).

[58] H. Fjellvag, A. Kjekshus, T. Chattopadhyay, H. D. Hochheimer, W. Hönle, and H. G. V. Schnering, Phys. Lett. A **112**, 411 (1985).

[59] P. Debye, Ann. Phys. (Berlin, Ger.) **348**, 49 (1913).

[60] I. Waller, Z. Phys. A **17**, 398 (1923).

[61] M. Esters, R. G. Hennig, and D. C. Johnson, Phys. Rev. B **96**, 235147 (2017).

[62] C. Ataca, H. Sahin, and S. Ciraci, J. Phys. Chem. C **116**, 8983 (2012).